Physica C: Superconductivity and its applications 532 (2017) 33–39

Contents lists available at ScienceDirect

Physica C: Superconductivity and its applications

journal homepage: www.elsevier.com/locate/physc

Amplitude distributions of dark counts and photon counts in NbN superconducting single-photon detectors integrated with the HEMT readout

J. Kitaygorsky[a,b], W. Słysz[c,*], R. Shouten[a], S. Dorenbos[a], E. Reiger[a], V. Zwiller[a,1], Roman Sobolewski[b,2]

[a] Kavli Institute of Nanoscience Delft, Delft University of Technology, 2600 GA Delft, The Netherlands
[b] Department of Electrical and Computer Engineering and Laboratory for Laser Energetics, University of Rochester, Rochester, NY 14627-0231, USA
[c] Institute of Electron Technology, PL-02 668 Warsaw, Poland

ARTICLE INFO

Article history:
Received 13 October 2016
Accepted 18 November 2016
Available online 30 November 2016

Keywords:
Single-photon detector
Superconducting nanostructure
Dark counts
Photon-number resolution
Superconducting single-photon detector
Cryogenic HEMT readout

ABSTRACT

We present a new operation regime of NbN superconducting single-photon detectors (SSPDs) by integrating them with a low-noise cryogenic high-electron-mobility transistor and a high-load resistor. The integrated sensors are designed to get a better understanding of the origin of dark counts triggered by the detector, as our scheme allows us to distinguish the origin of dark pulses from the actual photon pulses in SSPDs. The presented approach is based on a statistical analysis of amplitude distributions of recorded trains of the SSPD photoresponse transients. It also enables to obtain information on energy of the incident photons, as well as demonstrates some photon-number-resolving capability of meander-type SSPDs.

1. Introduction

Fast and reliable single-photon detectors (SPDs) have become a highly sought-after technology in recent years [1]. Some of the most interesting applications for SPDs, such as quantum communications and quantum key distribution [2], as well as satellite communications, require devices that can successfully operate at telecommunication wavelengths, namely1310 nm and 1550 nm. Another, very desirable features for ideal SPDs are their photon-number resolution (PNR) capability [3,4], for, e.g., all-optical quantum computing, and photon-energy sensitivity (PES) [5] for, e.g., spectral observations of so-called photon-starved objects. InGaAs avalanche photodiodes work at telecommunication wavelength and are commercially available; they do, however, suffer from severe after pulsing and require time gating, which limits their maximum count rate. Presently, they also lack the advanced PNR and PES capabilities [6,7].

It has already been established that nanostructured NbN superconducting SPDs (SSPDs) operate based on hotspot formation and bias current redistribution in ultra-thin (~4 nm), ultra-narrow (100 to 120 nm) and long (~0.5 mm) meandering NbN superconductive nanostripes [1,8]. NbN SSPDs have been shown to have counting rates exceeding 250 MHz, with reported quantum efficiencies (QEs) up to 57% [9] at 1550 nm wavelength and very low, < 10 Hz to 10 kHz, dark-count rates, depending on the operation bias point [10]. Typically, the SSPDs are kept at temperatures between 1.7 and 4.2 K (far below the NbN critical temperature T_C), and biased at currents I_{bias} close to the meandering stripe critical current I_C. Once a photon is absorbed by an NbN nanostripe, it breaks a Cooper pair, and, subsequently, a large number of quasiparticles are generated through the electron–electron and electron–phonon interactions, creating a local hotspot, where superconductivity is suppressed or even destroyed. The hotspot expels the supercurrent from its volume and forces it to flow near the stripe edges, where it can exceed the I_C value, leading to eventual formation of a resistive region (Joule heating) across the width of the stripe.

When the SSPD device is directly connected to a transmission line with the characteristic impedance Z_0 equal to, e.g., 50 Ω, the above-mentioned resistive region, which is typically $\gg 50$ Ω, forces the bias current to redistribute from the SSPD into the load, which means that under the voltage-source biasing, the amplitude of the

* Corresponding author.
E-mail address: wslysz@ite.waw.pl (W. Słysz).
[1] Also at the School Engineering Sciences, KTH Royal Institute of Technology, SE-100 44 Stockholm, Sweden.
[2] Also at the Department Physics and Astronomy and the Materials Science Program, University of Rochester, Rochester, NY 14627-0231, USA.

http://dx.doi.org/10.1016/j.physc.2016.11.008
0921-4534/

SSPD voltage response is always collected across the constant Z_0. The above conclusion is true even if the SSPD were illuminated by several photons and, consequently, several hotspots were simultaneously generated at various points along the meander. Thus, in the above experimental arrangement, which is actually typical for the vast majority of the published work, the SSPD photoresponse is insensitive to both the number and/or energy of incoming photons, and the device acts as a photon-event counter rather than an energy and/or spectrally sensitive detector.

We need to stress here that a biased SSPD can also generate output electrical pulses even when the input light is completely blocked and there are no photons incident upon the device. Those, so-called, dark-count pulses are transient voltage signals, spontaneously generated in a current-biased, long, superconducting nanostripe, and, when the device is connected to an output of a coaxial line, their amplitude is limited by Z_0 despite the fact that the physical origin of dark counts is very different from that responsible for photon counts. In the case of dark counts, the transient resistive state across the SSPD nanostripe is due to the current-induced generation and propagation of free vortex–antivortex pairs (VAPs) [11,12]. Thus, in experimental studies of the SSPD performance, it would be very important to be able to actually distinguish the photon counts from the dark counts.

The goal of this work is to show that, with our recently developed new readout scheme, which implements a low-noise cryogenic high-electron mobility transistor (HEMT) and a high-load resistor next to the detector [13], we are able, albeit not in real time, to resolve the difference between the SSPD dark- and photon-count events via collecting histograms of the output-pulse distributions, and, subsequently, comparing their mean amplitudes and distribution widths. We also present our early findings that demonstrate that same readout approach can lead to some PNR functionality in SSPDs, as it was predicted in [14]. We stress that although research presented here is rather preliminary, it does represent an important step towards making SSPDs true photon sensor-type devices with energy resolution.

Our paper is organized in the following way: the next Sec. provides a brief description of the SSPD fabrication process and presents our experimental setup based on the high-input-impedance HEMT read-out circuit. In Section 3, we discusses practical limitations of our, presented in Section 2, simple equivalent circuit of the SSPD, based on the fixed-equivalent-resistance hotspot model and the ability to fulfill the condition that the readout input impedance is always dominant. Section 4 presents our experimental data consisting of long, real-time SSPD traces collected either under photon illumination or in the dark. Next, we use a statistical approach for the data analysis to calculate the corresponding distributions functions. The comparison between the distributions' mean amplitudes and widths enables us to quantitatively distinguish photon absorption effects from dark counts. Finally, we analyze how experimental data collected by an SSPD directly connected to the high-impedance read-out can shed light on either the average photon number of the incident ultra-weak flux of monochromatic light, or provide some spectral characterization of multi-color pulses. Section 5 contains our summary and concluding remarks.

2. Device description and experimental setup

SSPDs were patterned from epitaxial-quality, 3.5-nm-thick NbN films, deposited by dc reactive magnetron sputtering onto sapphire substrates [15]. The films were characterized by a sheet resistance between 400 and 500 Ω/sq at room temperature, with T_C between 10 and 11 K, and the critical current density $J_C \approx 10^6$ A/cm2. The meander patterning was done by e-beam lithography and reactive ion etching. It is important to note here that, while the films were

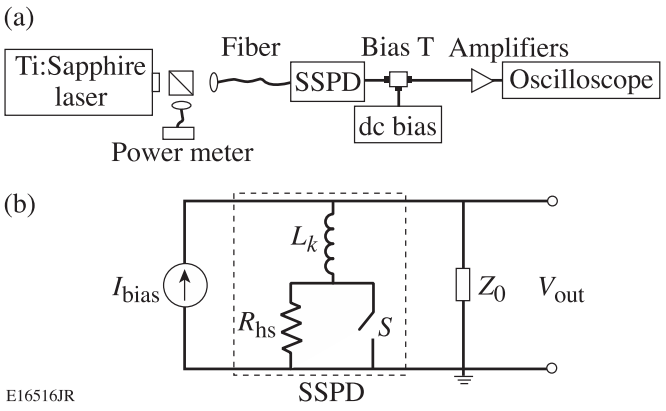

Fig. 1. (a) Experimental setup and (b) standard electrical photoresponse model of SSPD.

deposited at the Moscow State Pedagogical University, they were patterned at Delft University of Technology. Apparently, slight differences in geometry or in the patterning method were responsible for the fact that the SSPDs in this work had 3–4 times lower I_C's (~5 – 10 μA) than the typical Moscow devices [15]. The QEs, however, were on par with the standard 10×10-μm^2 SSPDs, with the devices measured in this work having QE ≈ 3–5 % at λ = 800 nm.

The standard SSPD operation setup is shown in Fig. 1(a). The device was wire bonded to a 50 Ω microstrip transmission line, coupled to a multimode optical fiber, and immersed into liquid helium [16]. The microstrip was then connected to a semi-rigid coaxial cable and at room temperature attached to a custom-made, wideband bias-tee (0.08–26-GHz bandwidth). The bias-tee enabled to simultaneously amplify the transient photoresponse signal using a tandem of two broadband amplifiers (0.08–8.5-GHz bandwidth, 22-dB gain), and DC bias both the SSPD and HEMT. The amplified output signals, corresponding to photon counts and/or dark counts, were recorded by using either a Tektronix digital single-shot oscilloscope (6-GHz bandwidth) or a pulse counter. As a photon source, we used a train of 100-fs-wide, 800-nm-wavelength pulses, generated by a mode-locked Ti:sapphire laser at a rate of 82 MHz The pulses were heavily attenuated in order to precisely control the average number of photons per pulse. For dark-count measurements, the detector was blocked from all incoming radiation, i.e., shielded inside the Dewar by a metallic enclosure. An equivalent electrical model of the SSPD photoresponse is shown in Fig. 1(b). Kinetic inductance L_k, is in series with a parallel arrangement of a hotspot resistance R_{hs} and a switch S represents the photodetection (switching) event in the SSPD [17]. The detector is then connected to a dc bias source and a readout circuit, which consists in this case of a transmission line with input impedance $Z_0 = 50\,\Omega$. Finally, V_{out} is the experimentally observed transient voltage pulse during photodetection.

Initially, the switch is closed, and there is no voltage drop. Once a photon is absorbed by our nanostripe, the switch opens, and as R_{hs} grows to a value much larger than Z_0, most of the current redistributes into Z_0, and the resultant voltage pulse amplitude is simply $V_{out} \approx Z_0(I_{bias} - I_{ret})$, where I_{ret} is the value of current flowing through the device at the highest value of R_{hs} [17]. Thus, independent of the number, or energy of the absorbed incident photons, and V_{out} always has the same value for a given I_{bias} for the circuit shown in Fig. 1(b).

Our high-impedance readout scheme, presented in Fig. 2, was first described in [13] and as already outlined there, it implements a commercial HEMT, operated cryogenically and mounted next (on the same board) to the SSPD. The HEMT acts as an infinite-impedance element to separate the 50 Ω output transmission line

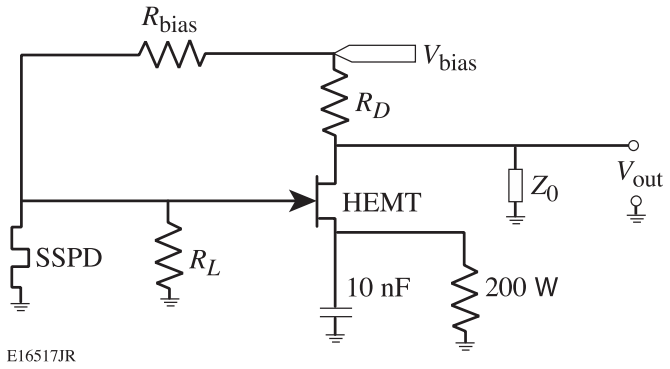

Fig. 2. SSPD circuit biasing and read-out schematics that implements a HEMT amplifier and a load resistor R_L. The 10-nF capacitor sets the maximum ac gain and the 200 Ω resistor sets the dc current for the HEMT; R_{bias} and R_D are the biasing and pull-up resistors, respectively.

from the SSPD. Because the HEMT input impedance is very high, an extra load (or shunt) resistor R_L is used in parallel with the detector [see Fig. 1(b) for SSPD schematics] and the HEMT. As we mentioned previously, both the SSPD and HEMT were biased through the same, custom-made, wideband bias-tee. Such an integrated arrangement enables a single bias, using $R_{bias} = 150\,k\Omega$, mounted on the board together with the rest of the components, and, simultaneously, to read out the ac photoresponse voltage signal. By applying the detector transient response to the gate of the HEMT, we can read out the drain voltage, which should, ideally (for $R_L \gg R_{hs}$), be proportional to the hotspot resistance and equal to V_{out}. If the number of photons simultaneously absorbed in the SSPD meander happens to be larger than 1, the photons are likely to form separate hot spots and their resistances will add up in series. The HEMT output voltage in this simplest case should be $V_{out} \approx (I_{bias} - I_{ret})nR_{hs}$, where n is the number of absorbed photons per pulse (actually, the number of created resistive regions). Therefore for relatively small n's and in the case of $nR_{hs} < R_L$, the output pulse height of our setup should be proportional to n, effectively leading to PNR, as it was theoretically discussed and modeled in [14].

Based on an intrinsic difference in the physics mechanisms of generation of photon and dark count transients in SSPDs discussed above, the HEMT setup should also enable one to distinguish pulses generated in response to either a single-photon absorption event (photon count) or a spontaneous voltage transient (dark count). In the case of dark counts, one can expect only a single localized resistive region, created by the VAP's motion across the stripe [12], with the effective resistance different than R_{hs}, resulting in a somewhat different value of V_{out}. In the full analogy, it is expected that photons of different energies should produce hot spots with different R_{hs} values, so our HEMT readout should possess PES functionality.

3. Readout circuit simulations and model limitations

Our HEMT approach takes the advantage of the simple fact that the greater R_L, the more sensitive the readout is in terms of either PRN or PES. Unfortunately, this cannot be easily accomplish since, the large R_L values lead to an under-damped circuit behavior, because of a very large value of the inductance ($L_k \sim 400$ nH) of our SSPD [17] in parallel with R_L. Fig. 3(a) shows the PSpice[3]-simulated pulses for different values of R_L, based on the circuits presented in Figs. 1(b) and 2. In the simulations, we also took into account (not shown in Fig. 2) a bandwidth of an outside (room temperature) amplifier. We note that as we increase the R_L values from 50 Ω to 2 kΩ the circuit response changes from heavily over-damped to heavily under-damped, respectively. The critical damping yields $R_L = 270\,\Omega$ [red dashed curve in Fig. 3(a)], while for $R_L = 500\,\Omega$ (green curve) the circuit is slightly under-damped.

Our tested SSPD's typically exhibited $I_C \approx 5\,\mu A$, leading to the roughly estimated R_{hs} value to be between 600 and 1000 Ω. Therefore, based on the behavior observed in Fig. 3(a), we selected $R_L = 500\,\Omega$ for all our experiments as a compromise between the optimal value (minimal oscillations) from the circuit point of view, and the need to have R_L as large as possible to achieve PNR functionality. Fig. 3(b) shows an experimental voltage pulse (black line) obtained using our HEMT readout with $R_L = 500\,\Omega$, as well as the corresponding PSpice-simulated fit (red dashed line). We note that while the fit, as we stressed above, represents the slightly under-damped condition, the slow oscillations visible on measured pulse are additionally associated with a small, second-order parasitic capacitance (not shown in Fig. 2) that comes from the HEMT mounting and/or stainless steel coaxial line, and was estimated to be 2 to 3 pF, by comparing with the oscillation frequency of the under-damped pulse.

Since $R_L = 500\,\Omega$ is at best comparable to R_{hs}, the experimentally measured V_{out} readout signal amplitude must be proportional to a parallel connection of R_L and R_{hs}, limiting our ability to fully, quantitatively distinguish between the different types of SSPD counting events. Therefore, the experimental observations presented here are mainly qualitative. In addition, since real-time analysis has been inconclusive, it was decided to use a statistical approach to analyze our experimental data. The approach of an SSPD integrated with an HEMT readout with a fixed $R_L = 500\,\Omega$ value can work satisfactorily, as will be shown later, but only for devices with rather small I_C and, consequently, typically, low QE. In large-QE SSPD's biased close to I_C, as shown in Ref. 18, the R_{hs} value can be as large as 5.5 kΩ, mainly because of Joule heating. Joule heating of the nanostripe turns it completely resistive and overpowers the hot-spot cooling process and current redistribution [18]. The latter can be well illustrated looking at the time-domain evolution of the photoresponse transient. Based on the electrical model shown in Fig. 2, the difference in amplitude for different hot-spot resistances stems from variations in the time interval it takes for the current initially biasing the device to redistribute into the readout circuit. In other words, for a given R_L, current redistribution time decreases with increasing R_{hs}. For the hotspot to stop growing and the cooling mechanism to take over, the current through the device must drop to a value below approximately 20% of I_C (Ref. 19). When the SSPD photoresponse is modeled such that R_{hs} is a simple resistor, the fall and rise time constants of the transient V_{out} are simply $\tau_{fall} = L_k/(R_{hs} + R_L)$ and $\tau_{rise} = L_k/R_L$ [17], respectively. On the other hand, if R_{hs} progressively increases during the current redistribution, the entire process becomes nonlinear and the transient decay cannot be modeled by a simple exponential function. From the readout circuit point of view, this is a very challenging problem since even if it were possible to find a cryogenic amplifier with large enough R_L, the readout scheme would not work because the current would not be able to redistribute into the load fast enough to prevent a runaway heating effect that would cause the device to latch. We believe the best approach to restrict the uncontrolled growth of R_{hs} and, consequently, suppress the heat runaway effect is to significantly improve the heat transport between the superconductor and the substrate, either by using substrates that have a better acoustic-phonon match to NbN, or by changing the nanostripe material. In the latter case, the ferromagnet/superconductor nanostructured bilayers are very promising because, as has recently been shown,

[3] PSpice (currently available from OrCAD Corp. of Cadence Design Systems, Inc.) is a PC version of SPICE originally developed at the Electronics Research Laboratory of the University of California, Berkeley (1975).

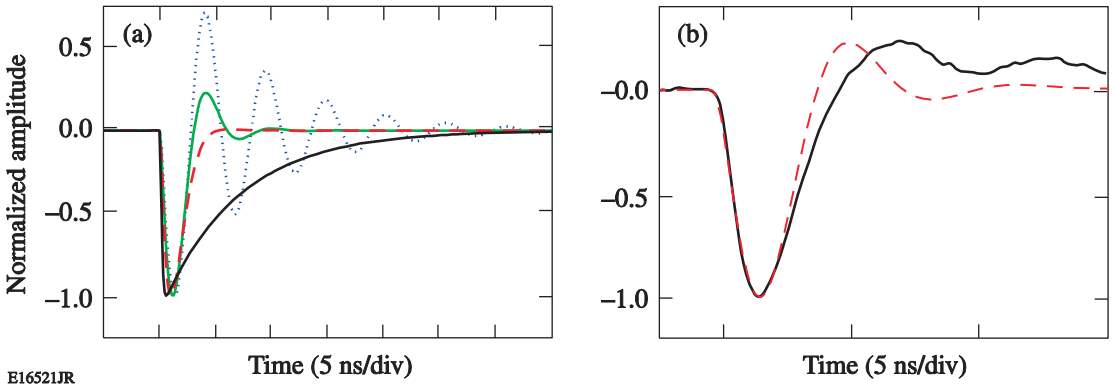

Fig. 3. (a) PSpice simulations of voltage transients at different values of R_L: 50 Ω (black curve), 270 Ω (red dashed curve), 500 Ω (green curve), and 2 kΩ (blue dotted curve). (b) An SSPD signal measured with the help of the HEMT readout (black curve) and the corresponding simulated photoresponse (red dashed curve), for $R_L = 500\ \Omega$. (For interpretation of the references to colour in this figure legend, the reader is referred to the web version of this article.)

they exhibit much-faster electron–phonon dynamics, as compared to plain Nb or NbN [20,21].

4. Results and discussion

During the course of our experiments, we have collected very long (millions of pulses), real-time traces by continuously recording either photon-count events or dark counts. In the latter case, the voltage response was measured when an SSPD was completely isolated from the outside world. Fig. 4(a) and (b) present randomly selected, short sections of photon-count traces of output pulses (after amplification) recorded in time-domain, when an SSPD was either connected according to the conventional 50 Ω scheme [Fig. 1(b)] or a scheme with an HEMT readout (Fig. 2), respectively. The incident laser intensity was adjusted in such a way that nearly every photon pulse was registered by the detector (for an SSPD with QE ≈ 5% that corresponded to +500 photons per pulse). These plots are intended to illustrate a qualitative difference in the recorded photoresponse signals, since even from such short "snapshots," it can clearly be seen that while in the case of the conventional biasing technique, pulse amplitudes remain constant, the HEMT readout allows one to record at least some quantitative differences between the different SSPD counting events.

For a more-quantitative analysis, a statistical approach was used to compute the distribution functions of amplitudes of pulses recorded under different experimental conditions. Fig. 5 shows histograms that compare pulse-amplitude distributions of dark counts [Fig. 5(a)], as well as the photon counts collected at two different laser intensities [Fig. 5(b) and (c)]. All data were taken using the HEMT readout and in each case the SSPD was biased using $I_{bias} = 0.9\ I_C$. All histograms were fitted with a simple Gaussian function and it is clear that the dark counts [Fig. 5(a)] exhibit the narrowest full-width-at-half-maximum (FWHM) distribution. For the photon counts, we observe a widening of the Gaussian distribution as we move from the single-photon regime [$n \sim 1$; Fig. 5(b)] to the multiphoton case [$n \geq 1$; Fig. 5(c)]. In principle, the observed increase in the width of the Gaussian distribution for the photon counts could have resulted from excess shot noise. To verify this hypothesis, we have additionally recorded a histogram (Fig. 6) of output pulses collected when the SSPD was operated under the same conditions as in Fig. 5(b), namely, in the single-photon ($n \sim 1$) regime; however, in that case, our detector was directly connected to a 50 Ω output line. We note that the histogram shown in Fig. 6 exhibits almost a perfect Gaussian distribution with a very narrow, noise-delimitated width. Therefore, the impact of the shot noise is negligible and we can conclude that, indeed, the HEMT readout allows one to get at least a quantitative insight on the amplitude variations of the SSPD voltage output pulses, when the device is operated under different experimental conditions, e.g., the different incident photon flux levels.

A large number of histograms of the type presented in Fig. 5 have been collected under different SSPD biasing and optical illumination conditions. The correlation between the photon flux (average number of photons per pulse) incident upon the detector and the FWHM of the resulting distribution of the response pulse amplitudes was very reproducible and has been summarized in

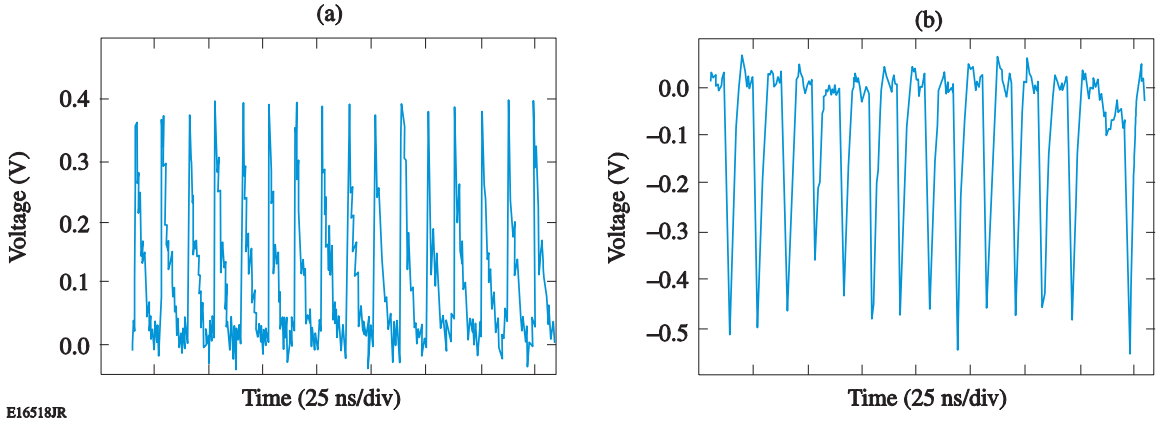

Fig. 4. Comparison of live oscilloscope time-domain traces for (a) a traditional scheme [Fig. 1(b)], and (b) an HEMT readout scheme (Fig. 2), taken at similar laser intensities, such that the number of absorbed photons per pulse $n \sim 1$. HEMT is an inverting amplifier; therefore the pulses in (b) are negative. The laser repetition rate is 82 MHz.

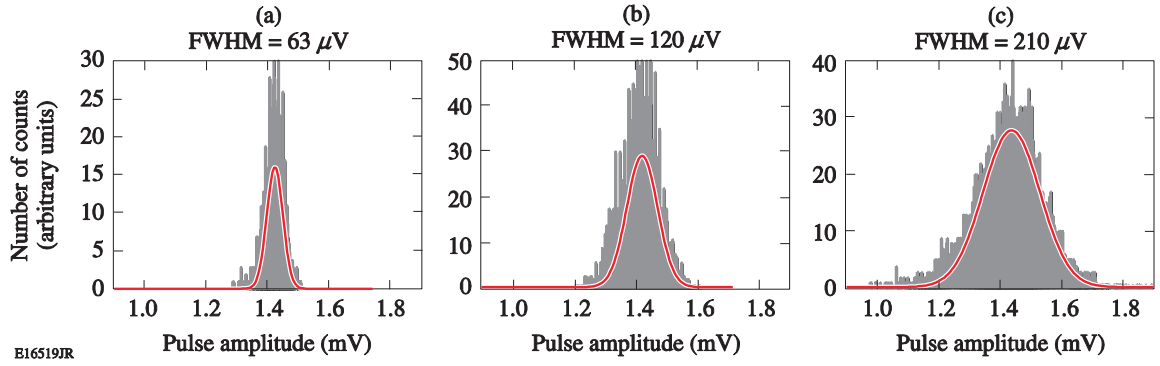

Fig. 5. (a) Pulse-amplitude histograms of dark counts, (b) photon counts in the single-photon regime $n \sim 1$, and (c) multiphoton regime $n \geq 1$. All measurements performed the HEMT readout at 4.2 K and at $I_{bias} = 0.9\ I_C$. The SSPD output-voltage amplitudes are divided by the amplifier gain.

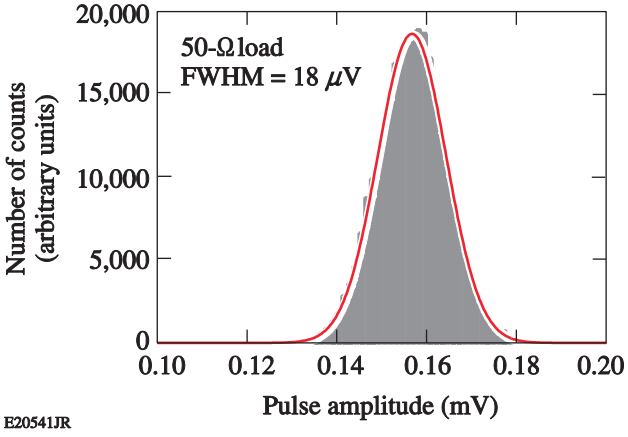

Fig. 6. Pulse-amplitude histogram of photon counts in the single-photon regime ($n \sim 1$), when the SSPD was directly connected to the 50 Ω output coaxial line (no HEMT readout). All measurements were performed at 4.2 K and $I_{bias} = 0.9\ I_C$. The SSPD output-voltage amplitudes are divided by the amplifier gain.

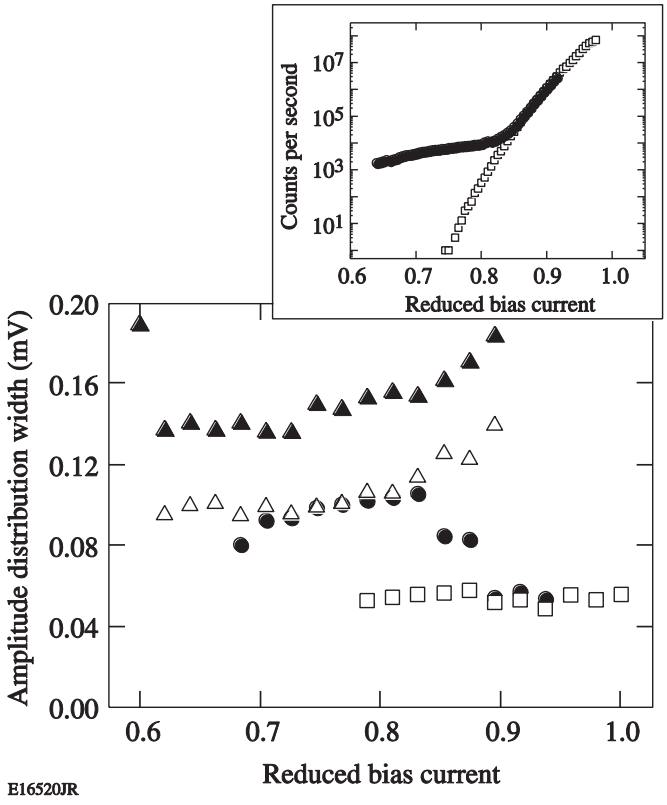

Fig. 7. Amplitude distribution width (FWHM of Gaussian fits) for dark counts (open squares) and photon counts with $n << 1$ (closed circles), $n \sim 1$ (open triangles), and $n \geq 1$ (closed triangles). The inset shows the counting rate as a function of the bias current for dark counts (open squares) and photon counts when $n << 1$ (closed circles).

Fig. 7, where the FWHM of the signal amplitude histogram versus the SSPD normalized current bias I_{bias}/I_C is presented, for both the dark counts (open squares) and the photon counts corresponding to the multiphoton ($n \geq 1$; closed triangles), single-photon ($n \sim 1$; open triangles), and heavily attenuated ($n \ll 1$; closed circles) illumination. We see that the dark-count signals exhibit the narrowest FWHM, which, in addition, is independent of the bias. On the other hand, substantial differences exist between the FWHM values corresponding to different incident photon fluxes. The general trend is that the distribution width increases with increasing I_{bias}/I_C, which is due to the increased SSPD sensitivity in the $I_{bias} \approx I_C$ biasing regime, where even photons hitting the edges of the nanostripe are likely to be counted [22]. On the other hand, for very low photon fluxes ($n \ll 1$; closed circles in Fig. 7), the amplitude distribution FWHM starts to drop around $I_{bias} = 0.83\ I_C$, eventually overlapping with the dark counts (open squares) at $I_{bias} > 0.9\ I_C$, as the dark-count events start to dominate over the photon counts. The latter behavior agrees very well with our earlier observation [11] of the near-exponential dependence of the rate of dark counts in SSPDs on the I_{bias}/I_C ratio and their dominance in the $I_{bias} \approx I_C$ limit, as shown in the inset in Fig. 7.

The significant difference (a factor of several) in the FWHM values of the histograms for the dark- and photon-count events collected for the SSPD with the HEMT readout must have come from the intrinsic difference in the physics of triggering those counts. As demonstrated in [12], when a current-biased SSPD is blocked from all incoming radiation (shielded by a metallic enclosure) and placed in liquid helium, the spontaneous transient voltage pulses, or dark counts, are primarily caused by topological excitations. The thickness of the NbN stripe is 3.5 nm and the width is ~100 nm, which puts the SSPD nanostripe in a two-dimensional (2-D) superconductor regime, because its thickness is smaller, but the width is larger than the NbN Ginsburg–Landau coherence length (~6 nm at $T = 0$ K). In 2-D systems, in general, true long-range superconducting order is not possible, and in an ultrathin film, topological excitations come in the form of VAP's [23]. For a typical nanostripe operating at temperatures far below T_C and in the absence of I_{bias}, all VAP's are bound and there is no dissipation (voltage drop) in the SSPD detector. Once I_{bias} is applied, it exerts a Lorentz force on VAP's, and at I_{bias} close to I_C, this force is strong enough to exceed the VAP binding energy and to break them. The latter effect cre-

ates free vortex and antivortex pairs—analogue to excited electrons and holes in semiconductors—and allows them to move in opposite directions toward the edges of the NbN stripe, causing dissipation and resulting in the resistive state [24]. Since the VAP breaking events originate exclusively at the "weakest" (narrowest and/or localized) constriction spots along the SSPD meander, the normal region produced from these events is going to have only minimal variations in the resistance and, consequently, the histogram of the corresponding voltage pulses is expected to exhibit a very narrow distribution.

The fact that the photon-count amplitude distributions (even in the single-photon regime) have FWHM's consistently wider than those corresponding to the dark counts can be well understood based on the hotspot driven photon-detection events. Photon absorption and resulting hotspot formation can happen at any point along the meander, leading to natural variations in the size of the resistive state [22]. Since the device I_C is determined by the narrowest and/or the thinnest section(s) of the nanostripe, fabrication-related fluctuations in the stripe's cross section (variations in the width and/or thickness of the NbN nanostripe are very likely to occur in our relatively low-QE SSPDs) must lead to R_{hs} variations that, in the case of our HEMT readout scheme, will be detected as the amplitude spread of photon-count responses. Finally, when the light intensity is relatively high ($n \geq 1$), multiphoton-absorption events are likely to happen, especially for I_{bias} approaching I_C, as more sections of the SSPD meander are activated. As a result, we should observe enhanced fluctuations in the response pulse amplitudes and, correspondingly, to the widest distribution FWHM, as, indeed, is visible in Figs. 5(c) and 7.

As it was mentioned before and predicted in [14], the integrated, cryogenic HEMT readout should not only allow one to distinguish dark counts from photon counts but also enable one to achieve PES and PNR in SSPD's. According to [14], a clear, real-time resolution between, e.g., the single- and two- or three-photon events, requires $R_L \gg R_{hs}$. Since in our readout design, we have decided to fix R_L to be equal to 500 Ω, the above condition is not strictly fulfilled in our experiments, as already discussed in Section 2, and we have to restrict ourselves to a statistical, post-processing analysis. Such an approach is obviously not practical for optical quantum computing but can find extended applications in, e.g., spectral characterization of unknown ultraweak light sources in astronomical observations.

We have already successfully implemented the statistical approach to demonstrate the SSPD PES capability in conventionally biased devices, where, by measuring the SSPD system's QE at different bias currents, we were able to resolve the wavelength of the incident photons with a resolution of 50 nm [5]. Using the statistical method, we have also earlier demonstrated that SSPD's operating in the HEMT readout configuration is able to distinguish photons of different energies [13]. Therefore, here we focus on the PNR capability of an SSPD connected directly to HEMT. As stressed before, in the case of devices with $I_C \approx 5$ μA and the HEMT $R_L = 500\,\Omega$, one should still be able to distinguish, at least qualitatively, between the single- and multiphoton events. Indeed, when the laser intensity and I_{bias} were increased so that the detector started to register nearly every incident light pulse while the dark counts were still low, one could observe that, in time-domain traces of the photoresponse counts, some pulses exhibited visibly higher amplitudes than the rest. Fig. 8 shows an example of such a real-time trace, which although convincing, is absolutely insufficient to conclude that these large pulses were indeed caused by double-photon events, instead of, e.g., a single-photon event arriving close in time to a dark-count event, or even resulting from a large inhomogeneity of the meandering nanostripe. It was, therefore, again necessary to look at the statistics of the pulse-amplitude distributions. This time, both the intensity of laser pulses and I_{bias} were varied for each case, and amplitudes of several million pulses were collected. Ultraviolet photons (frequency-doubled Ti:sapphire light) were used to increase the photon-detection efficiency of the SSPD.

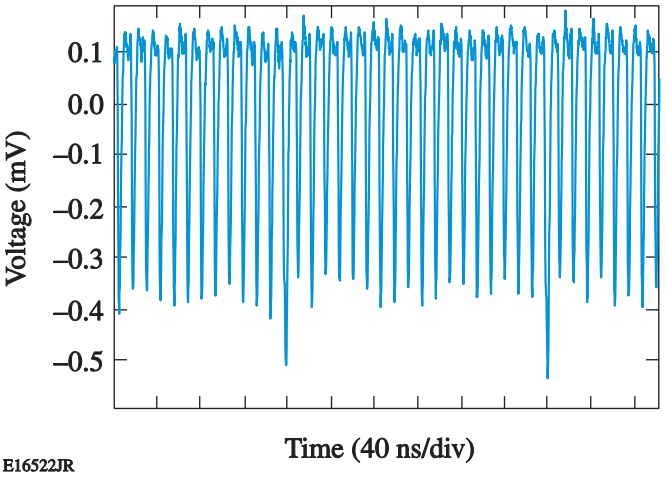

Fig. 8. Live oscilloscope time-domain trace, showing higher amplitudes of some pulses.

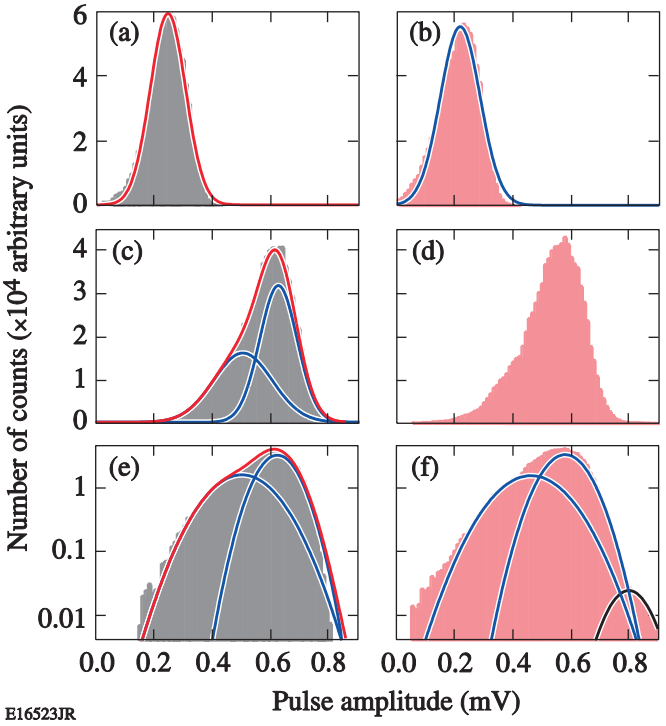

Fig. 9. Pulse-amplitude histograms for (a) $n << 1$, $I_{bias} = 0.7\ I_C$; (b) $n \leq 1$, $I_{bias} = 0.7\ I_C$; (c) $n << 1$, $I_{bias} = 0.9\ I_C$; (d) $n \leq 1$, $I_{bias} = 0.9\ I_C$; (e) semi-log plot of (c); and (f) semi-log plot of (d). Gray histograms indicate the incident photon flux for the $n << 1$ regime, while red histograms indicate the same incident photon flux but at the $n \leq 1$ regime. (For interpretation of the references to colour in this figure legend, the reader is referred to the web version of this article.)

The results are presented in Fig. 9. When $I_{bias} = 0.7 I_C$, the amplitude distribution can be fit with a simple Gaussian function, as shown in Figs. 9(a) and (b). Once I_{bias} has reached $0.9 I_C$, however, [as shown in Fig. 9(c) and (d)], one can see a substantial spreading of the distribution, which now has to be fitted with two Gaussians. Although the two-Gaussian distribution can be explained as a result of significant, non-uniform variations of the NbN stripe width, rather than a PNR phenomenon, a more-detailed analysis

of the presented plots favors the PNR interpretation. Figs. 9(e) and (f) show the same data as Figs. 9(c) and (d), respectively; however, they are re-plotted on a semi log scale. In Fig. 9(f) one can notice that, in the single photon ($n \leq 1$) regime, there is actually a third small Gaussian peak. This peak, however, is completely absent in the $n \ll 1$ regime [Fig. 9(e)]. This third peak also cannot be a result of dark counts since the dark counts are most pronounced in the case of $n << 1$ illumination, as demonstrated in Fig. 7. Taking into account that the mean amplitude of this third Gaussian peak is the largest, the most-reasonable, although tentative, explanation is that it is indeed a result of the SSPD detection of multiphoton events. Further detailed analysis is needed, however, to either support or disprove this conclusion.

5. Conclusion

In conclusion, we were able to observe the difference between dark counts and photon counts generated in our meander-type NbN SSPD's by utilizing an HEMT readout technique and, subsequently, examining distribution widths of the histograms of amplitudes of the collected in real-time dark- and photon-count signals. The distribution width for the dark count events was very narrow and independent of the bias current, while the FWHM of the distribution in the case of photon counts was up to 4 times wider and was directly related to the photon flux (the average number of photons per pulse) incident on the SSPD. The differences in the measured FWHM values of the output-pulse distributions could be satisfactorily explained by the different physical origin of the dark-count events (VAP breaking and Lorentz-force dissipation) and the photon-count events (photon-induced hot-spot formation). It has also been demonstrated that the HEMT readout offers a promise of PNR functionality in SSPD measurements. The next step in this direction is likely to come from implementing ferromagnet/superconductor bilayer nanostripes (e.g., NiCu/NbN heterostructures) that are not only characterized by picosecond quasiparticle-phonon relaxation dynamics but also exhibit almost an order-of-magnitude larger J_C value [25].

Acknowledgments

The authors thank Professor G. Gol'tsman and his group at the Moscow State Pedagogical University for their assistance in the sample preparation and Professor H. Mooij for very helpful discussions. Research in Rochester has been supported in part by the grant from the HYPRES Co., and by the New York State Advanced Technology Centers for Innovative and Enabling Technologies (University of Rochester) and Advanced Sensor Technologies (Stony Brook University). Research in Warsaw was supported by the Polish Ministry of Science under Project No. 4426/B/TO2/2007/33. We also acknowledge the European Union COST Action MP1201.

References

[1] W. Słysz, M. Węgrzecki, J. Bar, P. Grabiec, M. Górska, V. Zwiller, C. Latta, P. Böhi, I. Milostnaya, O. Minaeva, A. Antipov, O. Okunev, A. Korneev, K. Smirnov, B. Voronov, N. Kaurova, G. Gol'tsman, A. Pearlman, A. Cross, I. Komissarov, A. Verevkin, R. Sobolewski, Fiber-coupled detector based on NbN superconducting single-photon nanostructures for quantum communications, J. Mod. Opt. 54 (2007) 315–326.
[2] C.H.C.H. Bennett, G. Brassard, Quantum cryptography: "Public Key Distribution and Coin Tossing", in: International Conference on Computers, Systems, and Signal Processing, Bangalore, 1984, pp. 175–179.
[3] E. Waks, A. Zeevi, Y. Yamamoto, Security of quantum key distribution with entangled photons against individual attacks, Phys. Rev. A 65 (2002) 052310.
[4] E. Knill, R. Laflamme, G. Milburn, A scheme for efficient linear optics quantum computation, Nature 409 (2001) 46–52.
[5] E. Rieger, S. Dorenbos, V. Zwiller, A. Korneev, G. Chulkowa, I. Milostnaya, O Minayeva, G. Gol'tsman, J. Kitaygorsky, D. Pan, W. Slysz, A. Jukna, R. Sobolewski, Spectroscopy with nanostructured superconducting single-photon detectors, IEEE J. Sel. Topics Quant. Elec. 13 (2007) 934–943.
[6] Y. Kang, Y.-H. Lo, M. Bitter, S. Kristjansson, Z. Pan, A. Pauchard, InGaAs-on-Si single photon avalanche hotodetectors, Appl. Phys. Lett. 85 (2004) 1668–1670.
[7] G. Ribordy, N. Gisin, O. Guinnard, D. Stucki, M. Wegmuller, H. Zbinden, Photon counting at telecom wavelengthswith commercial In-GaAs/InP avalanche photodiodes: current performance, J. Mod. Opt. 51 (2004) 1381–1398.
[8] G.N. Gol'tsman, O. Okunev, G. Chulkova, A. Lipatov, A. Semenov, K. Smirnov, B. Voronov, A. Dzardanov, C. Williams, R. Sobolewski, Picosecond superconducting single-photon optical detector, Appl. Phys. Lett. 79 (2001) 705–707.
[9] K.M. Rosfjord, J.K.W. Yang, E.A. Dauler, A.J. Kerman, V. Anant, B. Voronov, G.N. Gol'tsman, K.K. Berggren, Nanowire Single-Photon Detector with an integrated optical cavity and anti-reflection coating, Optics Express 14 (2006) 527–534.
[10] J. Kitaygorsky, J. Zhang, A. Verevkin, A. Sergeev, A. Korneev, V. Matvienko, P. Kouminov, K. Smirnov, B. Voronov, G. Goltsman, R. Sobolewski, Origin of dark counts in nanostructured NbN single-photon detectors, IEEE Trans. Appl. Supercond. 15 (2005) 545–548.
[11] A. Engel, A. Semenov, H.-W. Hübers, K. Il'in, M. Siegel, Fluctuations and dark count rates in superconducting NbN single-photon detectors, Phys. Stat. Sol. C 2 (2005) 1668–1673.
[12] J. Kitaygorsky, I. Komissarov, A. Jukna, O. Minaeva, N. Kaurova, A. Korneev, B. Voronov, I. Milostnaya, G. Gol'tsman, R. Sobolewski, Dark counts in nanostructured NbN superconducting single-photon detectors and bridges, IEEE Trans. Appl. Supercond. 17 (2007) 275–278.
[13] J. Kitaygorsky, S. Dorenbos, E. Reiger, R. Schouten, V. Zwiller, R. Sobolewski, HEMT-based read-out technique for dark and photon count studies in NbN superconducting single-photon detectors, IEEE Trans. Appl. Supercond. 19 (2009) 346–349.
[14] M.G. Bell, A. Antipov, B. Karasik, A. Sergeev, V. Mitin, A. Verevkin, Photon number-resolved detection with sequentially connected nanowires, IEEE Trans. Appl. Supercond. 17 (2007) 289–292.
[15] G.N. Gol'tsman, K. Smirnov, P. Kouminov, B. Voronov, N. Kaurova, V. Drakinsky, J. Zhang, A. Verevkin, R. Sobolewski, Fabrication of nanostructured superconducting single-photon detectors, IEEE Trans. Appl. Supercond. 13 (2003) 192–195.
[16] W. Słysz, M. Węgrzecki, J. Bar, P. Grabiec, M. Górska, V. Zwiller, C. Latta, P. Böhi, I. Milostnaya, O. Minaeva, A. Antipov, O. Okunev, A. Korneev, K. Smirnov, B. Voronov, N. Kaurova, G. Gol'tsman, A. Pearlman, A. Cross, I. Komissarov, A. Verevkin, R. Sobolewski, Fiber-coupled single-photon detectors based on NbN superconducting nanostructures for practical quantum cryptography and photon-correlation studies, Appl. Phys. Lett. 88 (2006) 261113.
[17] A.J. Kerman, E.A. Dauler, W.E. Keicher, J.K.W. Yang, K.K. Berggren, G. Gol'tsman, B. Voronov, Kinetic-inductance-limited reset time of superconducting nanowire photon counters, Appl. Phys. Lett. 88 (2006) 111116.
[18] J.K.W. Yang, A.J. Kerman, E.A. Dauler, V. Anant, K.M. Rosfjord, K.K. Berggren, Modeling the electrical and thermal response of superconducting nanowire single-photon detectors, IEEE Trans. Appl. Supercond. 17 (2007) 581–585.
[19] A.V. Gurevich, R.G. Mints, Self-heating in normal metals and superconductors, Rev. Mod. Phys. 59 (1987) 941–999.
[20] T. Taneda, G.P. Pepe, L. Parlato, A.A. Golubov, R. Sobolewski, Time-resolved carrier dynamics and electron–phonon coupling strength in proximized weak ferromagnet/superconductor nanobilayers, Phys. Rev. B 75 (2007) 174507.
[21] D. Pan, G.P. Pepe, V. Pagliarulo, C. De Lisio, L. Parlato, M. Khafizov, I. Komissarov, R. Sobolewski, Layered ferromagnet/superconductor heterostructures: time-resolved femtosecond carrier dynamics and photodetector applications, Phys Rev B 78 (2008) 174503.
[22] A. Pearlman, A. Cross, W. Slysz, J. Zhang, A. Verevkin, M. Currie, A. Korneev, P. Kouminov, K. Smirnov, B. Voronov, G. Gol'tsman, R. Sobolewski, Gigahertz counting rates of NbN single-photon detectors for quantum communications, IEEE Trans. on Appl. Supercond. 15 (2005) 579–582.
[23] J.E. Mooij, Two-dimensional transition in superconducting films and junction arrays, in: A.M. Goldman, S.A. Wolf (Eds.), Percolation, Localization, and Superconductivity, 109, Plenum Press, New York, 1984, pp. 325–370.
[24] A.M. Kadin, Duality and fluxonics in superconducting devices, J. Appl. Phys. 68 (1990) 5741–5949.
[25] N. Marrocco, G.P. Pepe, A. Capretti, L. Parlato, V. Pagliarulo, G. Peluso, A. Barone, R. Cristiano, M. Ejrnaes, A. Casaburi, N. Kashiwazaki, T. Taino, H. Myoren, R. Sobolewski, Strong critical current density enhancement in NiCu/NbN superconducting nanostripes for optical detection, Appl. Phys. Lett 97 (2010) 092504-1-3.